Journal of Alloys and Compounds 708 (2017) 444–450

Contents lists available at ScienceDirect

Journal of Alloys and Compounds

journal homepage: http://www.elsevier.com/locate/jalcom

# Electrosprayed copper hexaoxodivanadate ($CuV_2O_6$) and pyrovanadate ($Cu_2V_2O_7$) photoanodes for efficient solar water splitting

Min-woo Kim [a, 1], Bhavana Joshi [a, 1], Hyun Yoon [b, 1], Tae Yoon Ohm [a], Karam Kim [a], Salem S. Al-Deyab [c], Sam S. Yoon [a, *]

[a] School of Mechanical Engineering, Korea University, Seoul, 136-713, Republic of Korea
[b] KIER-UNIST Advanced Center for Energy, Korea Institute of Energy Research (KIER), 50, UNIST-gil, Ulsan, 44919, Republic of Korea
[c] Petrochemical Research Chair, Chemistry Department, College of Science, King Saud University, P.O. Box 2455, Riyadh, 11451, Saudi Arabia

ARTICLE INFO

*Article history:*
Received 14 November 2016
Received in revised form
21 February 2017
Accepted 28 February 2017
Available online 2 March 2017

*Keywords:*
Copper vanadate oxide
Water splitting
Photocurrent
Photoanode

ABSTRACT

Copper hexaoxodivanadate ($CuV_2O_6$) and copper pyrovanadate ($Cu_2V_2O_7$) films were fabricated via electrostatic spray deposition for use as photoanodes for solar water splitting. The fabricated films were characterized by scanning electron microscopy, X-ray photoelectron spectroscopy, Raman spectroscopy, Transmission electron microscopy and X-ray diffraction analysis. The highest photocurrent density observed was 0.65 $mA \cdot cm^{-2}$ for a spraying time of 5 min in a mixed aqueous electrolyte consisting of 0.1 M borate and 0.1 M $Na_2SO_3$. The high photocurrent density is attributable to an improvement in the electrochemical kinetics at the electrode surface because of the scavenging holes from the electrolyte. The optimal annealing temperature was determined to be 500 °C. Further, $Cu_2V_2O_7$ was confirmed to be more suitable than $CuV_2O_6$ with respect to water splitting, as it exhibited a higher photocurrent density.


## 1. Introduction

Converting solar energy into electricity is a major scientific challenge and is being investigated extensively. Various metal oxide semiconductors such as $Fe_2O_3$, $Cu_2O$, $WO_3$, ZnO, $TiO_2$ and others, have been tested for use as electrode materials for photoelectrochemical (PEC) solar water splitting [1–3]. The required band gap energy of the photoelectrode must be 1.8–2.2 eV, in order for it to absorb the maximum amount of visible-light [4]. Further, the photoelectrode should produce a large number of photogenerated charge carriers, show high chemical stability, have high corrosion resistance, and be cost competitive. In addition, the positions of its conduction and valence bands should be such that they aid the absorption of as much visible light as possible [5,6]. Approximately 42–43% of the sunlight that reaches earth lies in the visible range. Hence, photoelectrodes capable of absorbing radiation in the visible-light region are of primary interest to the PEC research community [7].

Cuprous oxide ($Cu_2O$) is a p-type semiconductor oxide, having the bandgap range of 2.0–2.2 eV and thus is capable of absorbing the visible region of the spectrum. However, the limited stability of $Cu_2O$ has been one of the major drawbacks. Further, $Cu_2O$'s low migration rate of electrons and holes limits its applicability [8–10]. $WO_3$ and $Fe_2O_3$ are a photoanode material that is photoactive in the visible light region [11–13]. However, these materials have drawbacks of inefficient charge separation, short carrier diffusion length, and significant recombination.

To overcome these issues of the binary oxides, ternary oxides (three different elements) with a bandgap of <2.5 eV have been synthesized. Among the ternary oxides, metal vanadates such as $BiVO_4$, $InV_2O_4$, and $Ag_3VO_4$, have attracted considerable attention because they show excellent photocatalytic properties with respect to pollutant degradation and water splitting [14–18]. These metal vanadates are predicted to have band gaps and band alignments optimal for enhancing the solar absorption efficiency, making them highly suitable for solar water splitting applications [19,20]. Copper vanadate, an *n*-type material with a band gap of 2 eV, is one such metal vanadate and has been used in lithium-ion batteries, dye degradation, and water splitting [21,22].

Copper vanadium oxides (CVO) with different stoichiometries, such as $CuV_2O_6$ (hexaoxodivanadate), $Cu_2V_2O_7$ (pyrovanadate), and $Cu_3V_2O_8$, have been investigated; the latter two vanadates also exist as polytypes [19,23]. With respect to water splitting

* Corresponding author.
*E-mail address:* skyoon@korea.ac.kr (S.S. Yoon).
[1] These authors have contributed equally.

http://dx.doi.org/10.1016/j.jallcom.2017.02.302
0925-8388/

applications, every stoichiometric compound tested so far has exhibited a different photocurrent density (PCD). Recently, Seabold et al. [21] prepared a $Cu_3V_2O_8$ film (pseudolyonsite polymorph) by dip coating and used it as a photoelectrode for the oxygen evolution reaction (OER). Similarly, Cardenas-Morcoso et al. [24] reported the synthesis of chromium-doped copper vanadate ($Cr:Cu_3V_2O_8$) by the precipitation method and produced films of the compound by spin coating. These Cr-doped films exhibited a three-fold increase in the photocurrent (0.27 $mA{\cdot}cm^{-2}$) in borate buffer at 1.23 V (versus reversible hydrogen electrode (RHE)) as compared to pristine $Cu_3V_2O_8$. Guo et al. [25] reported that CVOs with the stoichiometries $CuV_2O_6$ and $Cu_2V_2O_7$ are suitable for use as active photoelectrocatalysts for the OER. They showed that $CuV_2O_6$ exhibits a PCD two times higher than that of $Cu_2V_2O_7$. Kawada et al. [26] reported that $CuV_2O_6$ shows the strongest catalytic activity with respect to the decomposition of $SO_3$ when the CVO is supported by $SiO_2$. However, they used this catalyst for hydrogen production through thermochemical water splitting and therefore did not report its PCD. Zhou et al. [19] used magnetron sputtering deposition to fabricate different types of $CuO\text{-}V_2O_5$ films, namely, those with McBirneyite ($\gamma\text{-}Cu_3V_2O_8$), ziesite ($\beta\text{-}Cu_2V_2O_7$), blossite ($\alpha\text{-}Cu_2V_2O_7$), and fingerite ($Cu_{11}V_6O_{26}$) phases. The McBirneyite film when annealed at 550 °C for 10 h showed a PCD value of 2 $mA{\cdot}cm^{-2}$ at pH 7 and 3 $mA{\cdot}cm^{-2}$ at pH 13. Sahoo et al. [27] produced *p*-type $Cu_3VO_4$ via the solid-state synthesis technique and used it as a photocathode material. However, the low charge efficiency of copper vanadate-based materials is the primary reason for their poor PEC performance. Further, vanadate-based materials readily undergo corrosion owing to the anodic dissolution of vanadium. In this regard, Zhou et al. [28] studied the PEC stability of copper vanadate photoanodes based on Pourbaix calculations and highlighted the role of borate buffer in the corrosion passivation of CVO films. Thus, borate buffer is now used widely as an electrolyte in studies on CVOs.

The aforementioned CVO films have been synthesized using hydrothermal [29], reactive sputtering [19], solid-state syntheses [27], sol-gel [30], drop casting [25], and dip coating [21] deposition methods. However, electrostatic spray deposition (ESD) has never been employed to deposit CVOs. Herein, for the first time, we used ESD to produce *n*-type $CuV_2O_6$ and $Cu_2V_2O_7$ films for use as photoanodes. ESD is a non-vacuum technique and comparable to the dip-coating and drop-casting methods used by Seabold and Neale [21] and Guo et al. [25], respectively. ESD can produce uniform submicrometer drops while consuming small amounts of the precursor; it has a deposition efficiency of nearly 100% [31] because the drops are guided by an electric field, allowing for accurate targeting. Furthermore, pyrolysis can be performed simultaneously with spraying by heating the substrate; during this stage, nanoscale structures are formed as the drops evaporate. The ESD spraying and annealing conditions were optimized to obtain uniformly coated and adhesive CVO films, which were then tested for use in PEC water splitting.

## 2. Experimental procedures

### 2.1. Setup for electrospraying and water splitting

The precursor for electrospraying was prepared by mixing copper (II) acetate ($Cu(CO_2CH_3)_2$, 1.19 g, Sigma-Aldrich), vanadium (III) acetylacetonate ($V(C_5H_7O_2)_3$, 1.49 g, Sigma-Aldrich), and propylene glycol ($CH_3CH(OH)CH_2OH$, 10 mL, Duksan) under stirring at 500 rpm for 20 min. The CVO films were deposited on indium tin oxide (ITO) substrates by ESD for spray times, $t_s$, of 1, 3, 5, and 10 min. The ESD conditions for fabricating the CVO films are listed in Table 1, while the setup used is shown in Fig. 1.

**Table 1**
Operating conditions of Copper vanadate oxide electrospraying.

| Items | Conditions |
|---|---|
| Substrate | Indium tin oxide (ITO) - coated glass |
| Applied voltage [kV] | 8.5 |
| ITO substrate dimensions [$cm^2$] | 2.5 × 2.5 |
| Distance nozzle to substrate [cm] | 4.5 |
| Coating time [min] | 1, 3, 5, 10 |
| Substrate temperature, [°C] | 150 |

### 2.2. Film characterization

X-ray diffraction (XRD) measurements (Rigaku, Japan, D/Max-2500) performed using Cu K$\alpha$ radiation over $2\theta$ values 20–40° were used to analyze the structures of the films. The chemical compositions of the film surfaces were studied using X-ray photoelectron spectroscopy (XPS, Theta Probe base system, Thermo Fisher Scientific Co.). The morphologies of the CVO films were studied using high-resolution scanning electron microscopy (HR-SEM, XL30 SFEG, Phillips Co., Holland) at 15 kV. Transmission electron microscopy (TEM) images and the corresponding selected-area electron diffraction (SAED) patterns of the films were recorded using a JOEL- 2100F system at an accelerating voltage of 200 kV. The TEM sample was prepared by the focused ion beam (5 nA, FIB, LYRA3 XMH, TESCAN) technique; cross-sectional samples were cut from the films to allow the cross-section to be imaged. The Raman scattering spectra of the CVO samples were measured using Raman spectrometer (LabRam ARAMIS IR2, Horiba Jobin Yvon) coupled with a 532-nm laser source.

### 2.3. Photoelectrochemical measurements

To determine the PEC performances of the CVO films, their PCD values were measured. A chemical reactor with three electrodes was used, as depicted in Fig. 1b. The CVO films were used as the working electrodes, while a Ag/AgCl electrode and a piece of Pt wire were employed as the reference and counter electrodes, respectively. In order to prevent a loss in ion mobility and ensure constant and accurate PEC results, the three electrodes were placed as close as possible to each other and fixed at these positions in the electrolyte. A 0.1 M borate buffer solution (pH = 9.2) was used as the electrolyte. A Xe arc lamp (Newport, Oriel Instruments, USA) equipped with an AM 1.5 filter set at an intensity of 100 $mW{\cdot}cm^{-2}$ was used as the light source to simulate sunlight. The photocurrent data were recorded using a potentiostat (VersaSTAT-3, Princeton Applied Research, USA), and the measurements were performed at a scan rate of 10 $mV{\cdot}s^{-1}$for applied voltages of 0.0–1.2 V (versus Ag/AgCl).

## 3. Results and discussion

### 3.1. Film morphology

Fig. 2a shows SEM images of the CVO films formed for spraying times of 1–10 min. For $t_s$ = 1 min, the CVO particles are spread uniformly on the substrate. Further, it can be seen that the average grain diameter ranges from 100 nm to 2 μm. The particles become stacked irregularly as the spraying time is increased from 3 min to 10 min, with the grain size increasing to ~20 μm for the 10-min case. The film formed for $t_s$ = 1 min is planar. Further, in the case of the films formed for $t_s$ = 3 and 5 min, the surfaces are rough, providing sufficient reaction sites for PEC activity. However, for the film formed for $t_s$ = 10 min, the particles are too large, resulting in a reduction in the surface area. The cross-sectional views of the films,

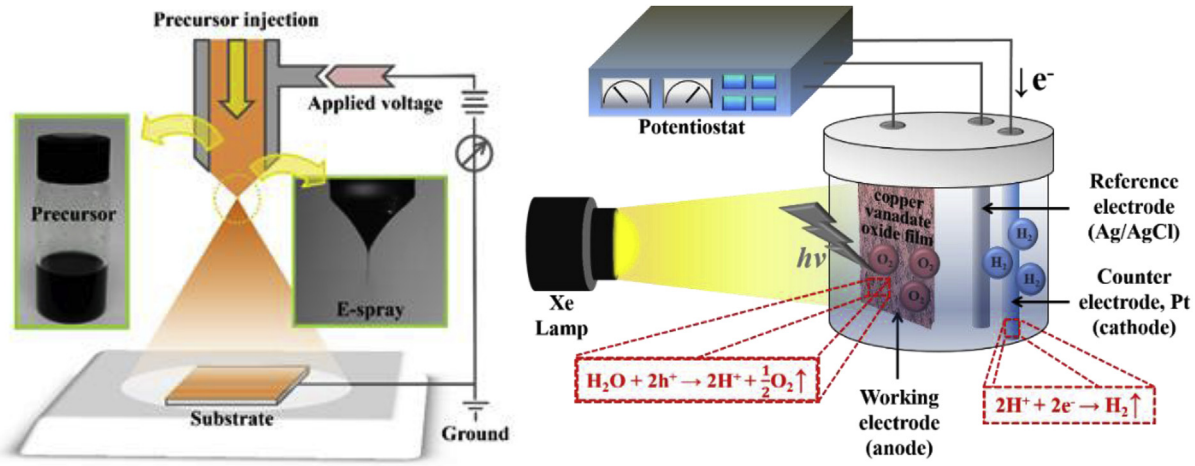


**Fig. 1.** (a) Schematic of electrospraying process used for synthesizing CVO films and (b) setup for water splitting.

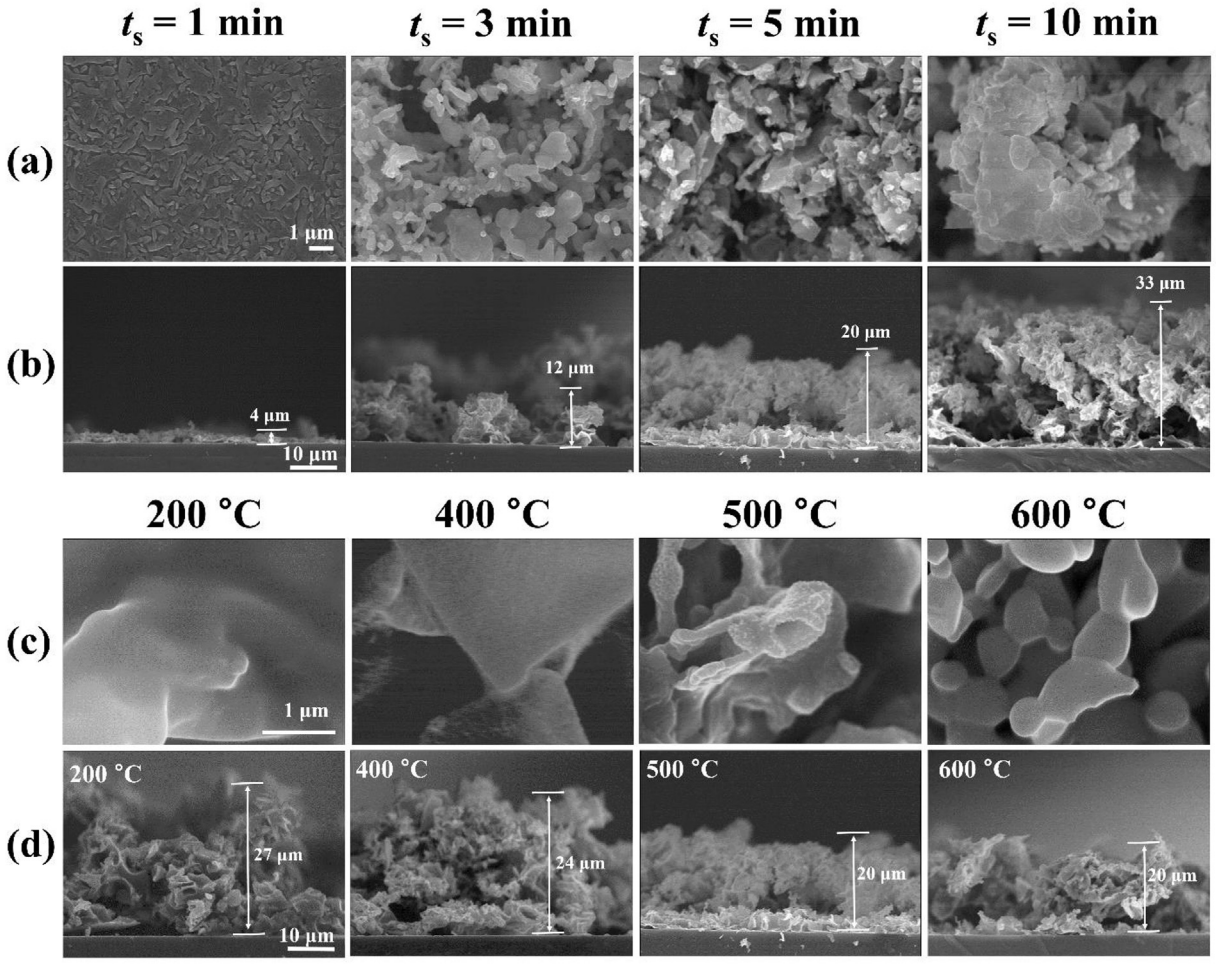


**Fig. 2.** SEM images of $Cu_2V_2O_7$ films synthesized for different ESD times at 500 °C annealing temperature: (a) surface view and (b) cross-sectional view and thickness. SEM images of CVO films annealed at different temperatures for $t_S$ = 5 min: (c) surface view and (d) cross-sectional view.

shown in Fig. 2b, indicate the same trends. The thickness of the films increases from 2 μm in the case of the film corresponding to $t_s$ = 1 min to 20 and 33 μm for the films corresponding to $t_s$ = 5 and 10 min, respectively. Thus, the images in Fig. 2a and b confirm that films with porous and rough microstructures are formed for deposition times in the range $3 \leq t_s \leq 5$ min while thicker films with an irregular and puffy morphology are obtained for $t_s > 5$ min.

SEM images of the CVO films annealed at 200–600 °C are shown in Fig. 2c. The morphology of the film annealed at 200 °C is nongranular. However, it can be seen that grains start forming at

400 °C. A few crystals can be seen clearly in the film annealed at 500 °C. However, no crystals are present in the film annealed at 600 °C. In addition, this film exhibits smaller, rounder grains. Fig. 2d shows the thicknesses of the films annealed at 200–600 °C. The thickness of the film annealed at 200 °C is 27 μm, but that of the films annealed at 500 and 600 °C is 20 μm. This decrease in the thickness is due to the high annealing temperature, which results in the removal of organic impurities through evaporation.

### 3.2. XPS and Raman spectroscopy

XPS was used to determine the chemical and electronic structures of the CVO films annealed at 500 °C. The binding energies of the Cu 2*p*, V 2*p*, O 1*s*, and C 1*s* orbitals are shown in Fig. 3a. The binding energies of Cu, considering the spin-orbital splitting of the 2*p* core level, are 933.6 and 953.1 eV and are attributable to the Cu $2p_{1/2}$ and Cu $2p_{3/2}$ doublet peaks, respectively, as illustrated in Fig. 3a. The binding energy difference between the Cu $2p_{3/2}$ and $2p_{1/2}$ peaks is approximately 19.5 eV [32], suggesting that Cu is present in the Cu (I) state. In addition to the Cu $2p_{3/2}$ and $2p_{1/2}$ peaks, two additional peaks are observed at binding energies of 941.3 and 961.5 eV; these are indicative of an open $3d^9$ shell corresponding to the $Cu^{2+}$ state. The peaks for V $2p_{3/2}$ (517.3 eV) and V $2p_{1/2}$ (524.7 eV) can be indexed to $V^{5+}$. These results match well with those reported previously [33]. Thus, Cu and V coexist in the film in the form of $Cu^{2+}$ and $V^{5+}$, respectively. The O 1*s* peak occurs at 529.75 eV, confirming the presence of oxygen in the film. The CVO film was annealed at a high temperature, resulting in the decomposition of the impurities from the organic sources. Thus, the carbon peaks observed in XPS are due to unavoidable environmental contamination inflicted during the sample preparation for XPS.

The chemical structures of the CVO films were confirmed based on the Raman scattering data shown in Fig. 3b. The Raman spectra were measured for wavenumbers of 100–1200 $cm^{-1}$. The Raman peaks observed at 388, 546, 741, 785, and 904 $cm^{-1}$ can be attributed to the vibrations of the bonds in $CuV_2O_6$, while those seen at the higher wavenumbers, such as those at 729, 846, 913, and 960 $cm^{-1}$, are ascribable to $Cu_2V_2O_7$. The CuO peaks are also present in the case of the film annealed at 500 °C, along with those related to the $Cu_2V_2O_7$ phase. This coexistence of multiple phases was also reported by Newhouse et al. [34], who suggested that it may be difficult to detect CuO in mixed phases, as in this case.

To gain further insight into the characteristics of the CVO films, TEM imaging and SAED pattern analysis were performed on the CVO films annealed at 500 °C and 600 °C; the results are shown in Fig. 4. The TEM images in 4a,b are cross-sectional views of the films, obtained using samples produced by FIB milling. As can be seen from Fig. 4c, the SAED pattern of the film annealed at 500 °C contains diffraction spots that can be indexed to the (310), (020), and (200) crystalline planes of $Cu_2V_2O_7$, confirming the presence of $Cu_2V_2O_7$. Further, $CuV_2O_6$ is also present, as evidenced by the spots related to its (310) and (111) planes (see Fig. 4c). This confirms the coexistence of the two phases in the film annealed at 500 °C. Further, the SAED pattern of the film annealed at 600 °C, shown in Fig. 4d, exhibits diffraction spots that can be indexed to the planes of $CuV_2O_6$ ((201), (111), (003), and (403)), $Cu_2V_2O_7$ ((150), (223), (202), and (021)), and CuO ((020), (111), and (312)). Thus, three phases were observed in the film annealed at 600 °C, in keeping with the XRD data, which are discussed later.

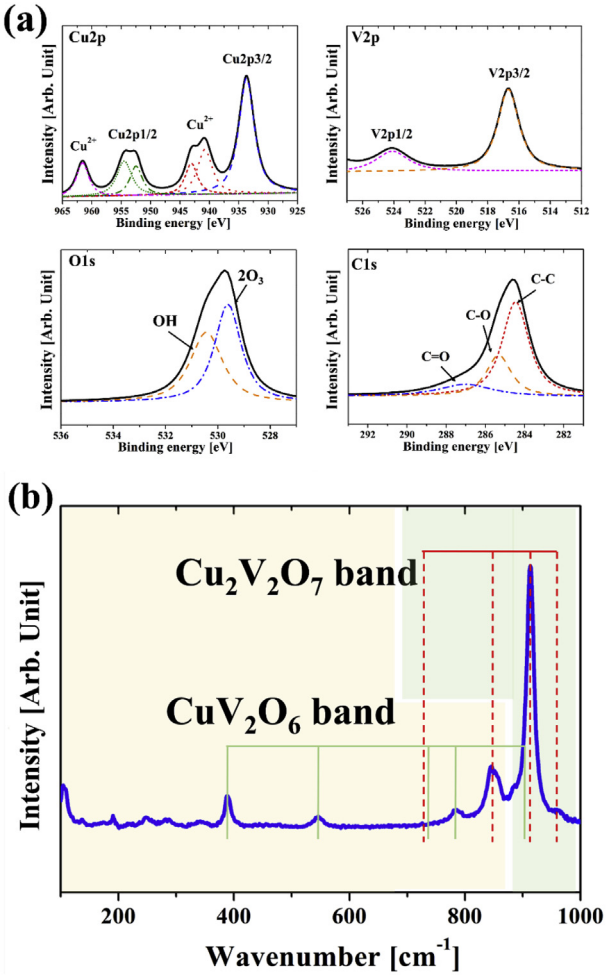


**Fig. 3.** (a) XPS Cu 2*p*, V 2*p*, O 1*s*, and C 1*s* spectra of $Cu_2V_2O_7$ and (b) Raman spectrum of $Cu_2V_2O_7$ film fabricated for spraying time of 5 min.

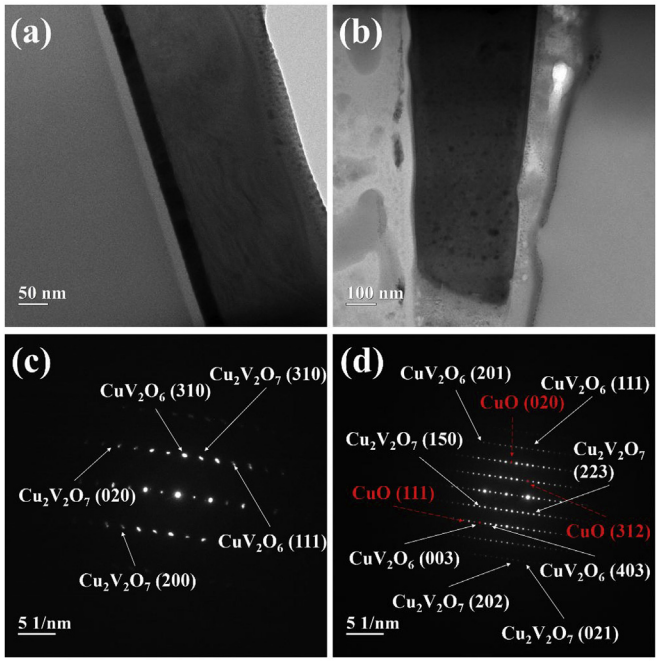


**Fig. 4.** (a) and (b) Cross-sectional TEM images of films annealed at 500 and 600 °C and (c) and (d) their SAED patterns.

### 3.3. Effects of annealing

The XRD patterns of the CVO films annealed at temperatures of 200–600 °C are shown in Fig. 5a. CVO-related peaks are not visible after annealing at temperatures of 200–400 °C. The diffraction peaks related to ITO are observed at 2$\theta$ of 21.31°, 30.37°, and 35.25°. Further, CVO-related peaks are detected in the films annealed at temperatures of 500 °C and higher. The peaks at 2$\theta$ of 20.63°, 26.67°, 27.61°, 29.34°, 31.63°, and 33.67° are attributable to $CuV_2O_6$ (PDF#16-0127), while the peaks at 2$\theta$ of 24.53°, 26°, 28.77°, and 33.67° correspond to $Cu_2V_2O_7$ (PDF#73-1032) [32]. Guo et al. [25] also reported that the $Cu_2V_2O_7$ phase is present in CVO films annealed at 500 °C when the Cu/V ratio is 1:1. The XRD pattern of the film annealed at 500 °C confirms the presence of the two phases. Further, when the annealing temperature is increased to 600 °C, the $CuV_2O_6$ phase becomes dominant. A few CuO-related peaks are also observed in this film, as represented by the open diamonds ( ◇ ), along with $CuV_2O_6$-related peaks. The peak at 2$\theta$ of 26°, which is ascribable to the $Cu_2V_2O_7$ phase, disappears in the case of the film annealed at 600 °C. Thus, it can be concluded that increasing the annealing temperature results in the transformation of the CVO from $Cu_2V_2O_7$ into $CuV_2O_6$ as well as the formation of CuO; this is what lowers the PEC performance.

As mentioned in the Experimental section, the PEC performances of the films were evaluated using a three-electrode cell under AM 1.5 illumination from the front side of the working electrode in 0.1 M Borate buffer. Fig. 5b shows the measured potentials both versus an RHE and versus a Ag/AgCl electrode. $E_{RHE}$ is the potential versus the RHE while $E_{Ag/AgCl}$ is the potential versus the Ag/AgCl electrode ($E_{RHE} = E_{Ag/AgCl} + 0.059pH + E_{0,Ag/AgCl}$) [35]. Based on the XRD analysis results, the PCD values of the CVO films annealed at 500 °C and 600 °C were measured; the results are shown in Fig. 5b. The obtained current density–voltage curves are indicative of an *n*-type photoanode, suggesting that the photocurrent is generated by oxygen evolution, as per the OER mechanism. For both films, the spraying time was 5 min. The sample annealed at 500 °C exhibits the highest PCD, which is 0.1 mA·cm$^{-2}$, at 1.23 V (versus RHE). On the other hand, the sample annealed at 600 °C shows a PCD of 0.04 mA·cm$^{-2}$ at 1.23 V (versus RHE). Thus, the sample annealed at 500 °C, in which the $Cu_2V_2O_7$ phase is dominant, exhibits better PEC performance.

### 3.4. Effect of electrospraying time on photocurrent density

Fig. 6 shows the XRD patterns of the CVO films fabricated using spraying times of 1, 3, 5, and 10 min. The peaks at 2$\theta$ of 24.53°, 26°, 28.77°, and 33.67° in the case of the film annealed at 500 °C (denoted by the filled black diamond symbols) correspond to $Cu_2V_2O_7$ and are in agreement with those shown for the films annealed at 500 °C in Fig. 6. On the other hand, the weak peaks at 2$\theta$ of 20.63°, 26.67°, 27.61°, 29.34°, 31.63°, and 33.67° are attributable to $CuV_2O_6$. The diffraction peaks marked with the black vertical lines are related to the ITO substrate. The increase in the sharpness and intensity of the CVO-related peaks in the XRD patterns with an increase in the spraying time indicates that the crystallinity of the CVO films increases with the spraying time and film thickness (see Fig. 2). However, higher-intensity peaks, that is, greater crystallinity, do not necessarily indicate enhanced solar water splitting performance, which primarily depends on the surface morphology and the number of reaction sites available for PEC activity.

Fig. 7 shows the current–voltage curves recorded at a scan rate of 10 mV·s$^{-1}$ for films formed using different spraying times. The curves were measured using two different electrolytes: **(a)** 0.1 M borate buffer and **(b)** 0.1 M borate with 0.1 M sodium sulfite

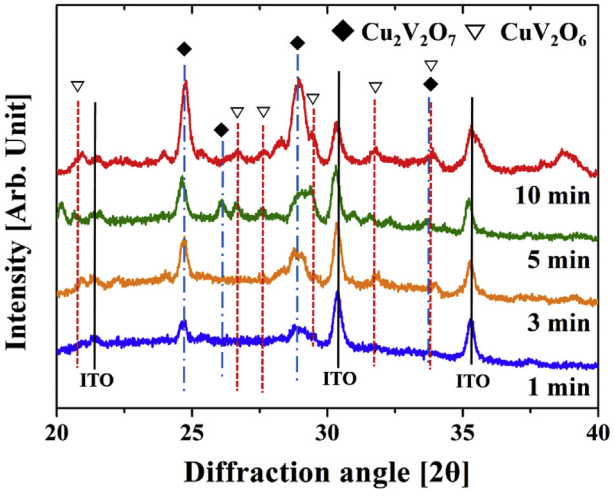


**Fig. 6.** XRD patterns of CVO films electrosprayed for different times ($t_S$) and annealed at 500 °C.

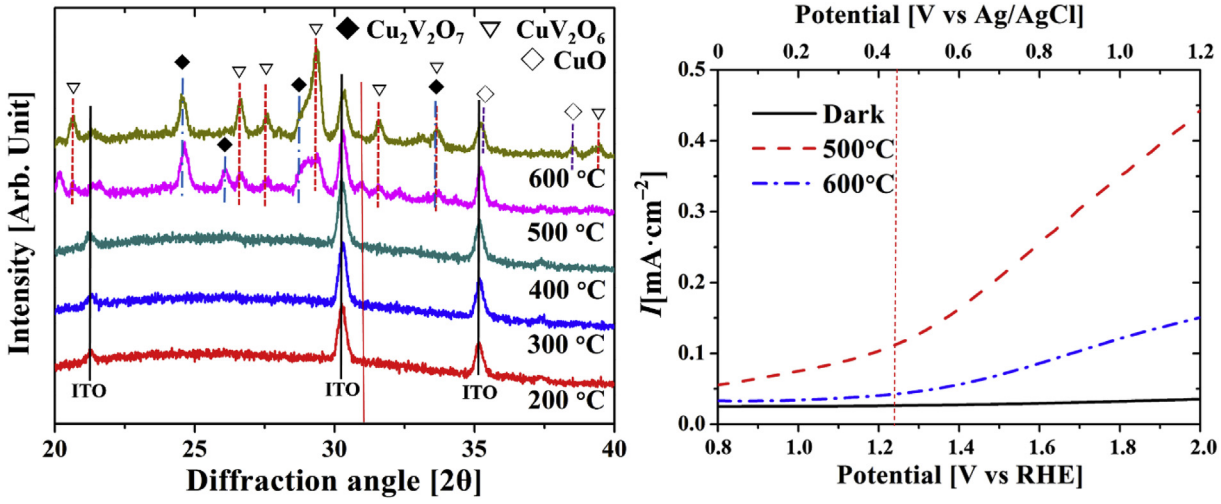


**Fig. 5.** (a) XRD patterns of CVO films annealed at various temperatures and (b) current–voltage (I–V) curves of films annealed at 500 and 600 °C and at $t_S$ = 5 min.

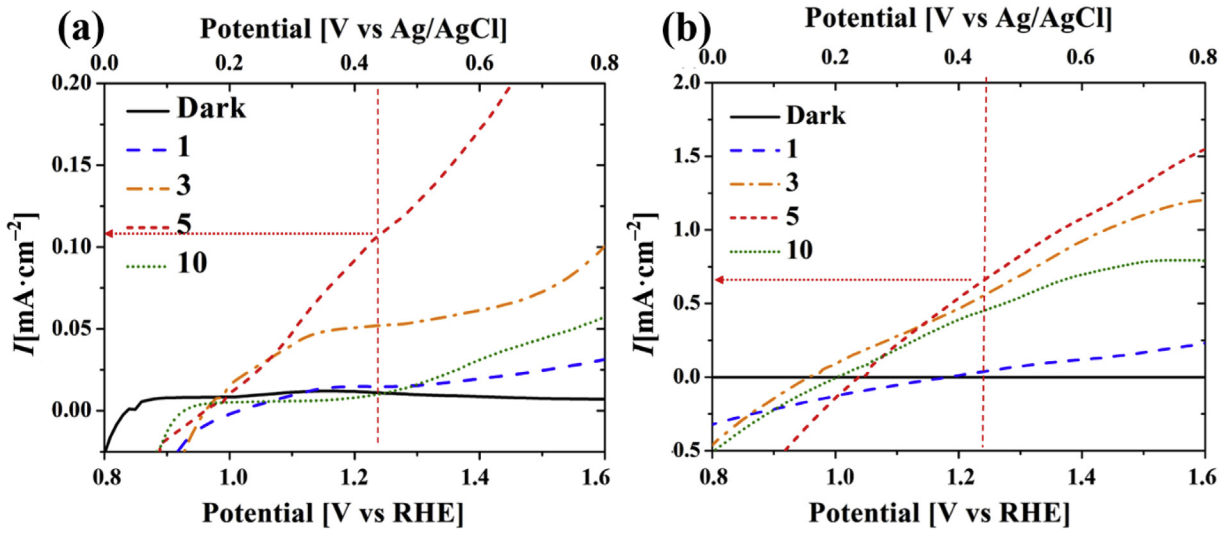


**Fig. 7.** Effect of electrospraying time on PCD for various electrolytes: (a) 0.1 M Borate and (b) 0.1 M Borate + 0.1 M Sodium sulfite. The annealing temperature for the films was 500 °C.

($Na_2SO_3$ or SS). The PCD values measured using the second electrolyte (borate + $Na_2SO_3$) are higher, confirming that the PCD is affected by the electrolyte used.

The dark current remains nearly zero for potentials up to 1.6 V (versus RHE); the corresponding PCD is shown in Fig. 7. The PCD value increases with the spraying time till $t_s = 5$ min (film thickness of 20 μm)—this is true for both electrolytes. The reason for this is that an increase in the spraying time improves the film surface morphology, as shown previously in Fig. 2. However, for $t_s > 5$ min, the film thickness increases to 33 μm, which reduces the surface area and hence the number of PEC reaction sites available. As a result, the PCD value in the case of the film corresponding to $t_s = 10$ min is significantly lower. The highest PCD value, which is observed in the case of the film corresponding to $t_s = 5$ min, is attributable to its light absorbance and electron–hole pair generation rate being the highest. Conversely, the thicker film, that, is the film formed for $t_s = 10$ min, has a longer transport path for the charge carriers, which decreases the effective electric field, permitting the rapid recombination of the electron–hole pairs and resulting in poor PCD performance. Therefore, the optimal deposition time is determined by the trade-off between the increase in the light absorbance and the simultaneous increase in the transport distance for the photogenerated charge carriers.

We would like to note that the PCD value obtained using $Na_2SO_3$ (see Fig. 7b) is much higher than that reported by Guo et al. [25] for $Cu_2V_2O_7$. Hole scavengers such as $Na_2SO_3$ have been used previously (see references in Table 2) to minimize surface recombination in metal oxides and maximize water oxidation. When $Na_2SO_3$ is used as the electrolyte, the PCD is 0.65 mA·cm$^{-2}$ at 1.23 V (versus RHE), which is comparable to the other values listed in Table 2, highlighting the superiority of the electrosprayed CVO films synthesized in this study.

The water splitting reaction rate and amount of photocurrent generated under solar illumination are proportional to the volume of oxygen evolved. The mechanism underlying the water splitting and oxygen evolution process is described in Fig. 8. Because the conduction band edge potential of CVO is lower than the oxygen evolution potential, CVO acts as an OER electrode, which is a photoanode. Under solar illumination, electrons are generated in the CVO and transported to the counter electrode, which uses these electrons to produce hydrogen, while the holes are used to produce oxygen at the anode. The PCD value exhibits a significant dependence on the reaction kinetics at the electrode surface [21]; slower kinetics can hinder oxygen generation and even cause peroxide

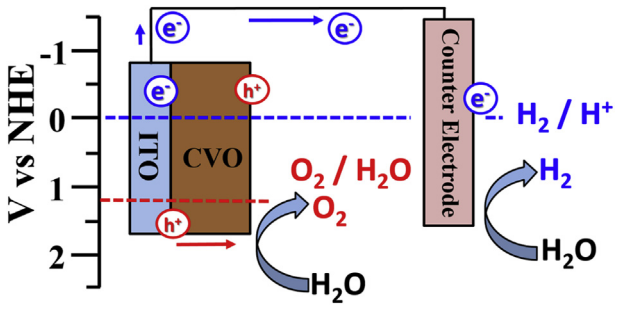


**Fig. 8.** Mechanism of water splitting by CVO.

**Table 2**
Comparison of the PEC performances of the present copper vanadate oxide thin films fabricated by non-vacuum processes.

| CVO type | Method/Substrate | Electrolyte | PCD [mA·cm$^{-2}$] @1.23V RHE | Onset potential | Ref. |
|---|---|---|---|---|---|
| $Cu_3V_2O_8$ | Dip coating/FTO | $0.1M^{PB} + 0.1M^{SS}$ | 0.28 | 0.70 | [21] |
| $CuV_2O_6$ | Drop casting/FTO | $0.1M^{SB} + 0.1M^{SS}$ | 0.25 | 0.80 | [25] |
| $Cu_2V_2O_7$ | Drop casting/FTO | $0.1M^{SB} + 0.1M^{SS}$ | 0.12 | 0.75 | [25] |
| **$Cu_2V_2O_7$** | **Electrospray/ITO** | **$0.1M^{B} + 0.1M^{SS}$** | **0.65** | **1.05** | **Present** |

PB = Potassium Borate.
SB = Sodium Borate.
SS = Sodium Sulfite.
B = Borate.

formation in some cases, which further promotes charge recombination [36]. This can be prevented by using a hole-scavenging electrolyte such as $Na_2SO_3$ [25]. This concept has been demonstrated previously by Seabold and Neale [21] and Guo et al. [25]. The sulfite oxidation reaction that occurs at the CVO surface under solar illumination is as follows [36,37]:

$$SO_3^{2-} + H_2O \rightarrow SO_4^{2-} + 2H^+ + 2e^-$$

## 4. Conclusions

Superior water splitting performance was achieved using ESD CVO films. The maximum photocurrent observed was 0.65 $mA \cdot cm^{-2}$ for the film fabricated using a spraying time of 5 min and a mixed aqueous electrolyte consisting of 0.1 M borate and 0.1 M $Na_2SO_3$. The optimal annealing temperature was determined to be 500 °C, as annealing at this temperature produced films containing both $CuV_2O_6$ and $Cu_2V_2O_7$ phases. The surface morphology of the films had a significant effect on the PCD; smaller crystal sizes with a greater numbers of reaction sites led to a higher PCD, whereas larger crystals lowered the PCD. The film thickness also affected the phenomena of light absorption and charge recombination.

## Acknowledgement

This research was supported by Global Frontier Program through the Global Frontier Hybrid Interface Materials (GFHIM) of the National Research Foundation of Korea (NRF) funded by the Ministry of Science, ICT and Future Planning (2013M3A6B1078879). This research was also supported by the Technology Development Program to Solve Climate Changes of NRF-2016M1A2A2936760. S.S. Yoon expresses his appreciation to the Vice Deanship of Scientific Research chairs at King Saud University for the partial support to this work.

## References

[1] F. Xu, J. Mei, M. Zheng, D. Bai, D. Wu, Z. Gao, K. Jiang, Au nanoparticles modified branched $TiO_2$ nanorod array arranged with ultrathin nanorods for enhanced photoelectrochemical water splitting, J. Alloys Compd. 693 (2017) 1124–1132.
[2] A. Ray, I. Mukhopadhyay, R. Pati, Y. Hattori, U. Prakash, Y. Ishii, S. Kawasaki, Optimization of photoelectrochemical performance in chemical bath deposited nanostructured CuO, J. Alloys Compd. 695 (2017) 3655–3665.
[3] G. Wang, Y. Yang, Y. Ling, H. Wang, X. Lu, Y.-C. Pu, J.Z. Zhang, Y. Tong, Y. Li, An electrochemical method to enhance the performance of metal oxides for photoelectrochemical water oxidation, J. Mater. Chem. A 4 (2016) 2849–2855.
[4] M.G. Mali, H. Yoon, B.N. Joshi, H. Park, S.S. Al-Deyab, D.C. Lim, S. Ahn, C. Nervi, S.S. Yoon, Enhanced photoelectrochemical solar water splitting using a platinum-decorated CIGS/CdS/ZnO photocathode, ACS Appl. Mater. Interfaces 7 (2015) 21619–21625.
[5] S. Ariffin, H. Lim, Z. Talib, A. Pandikumar, N. Huang, Aerosol-assisted chemical vapor deposition of metal oxide thin films for photoelectrochemical water splitting, Int. J. Hydrogen Energy 40 (2015) 2115–2131.
[6] R. Marschall, Semiconductor composites: strategies for enhancing charge carrier separation to improve photocatalytic activity, Adv. Funct. Mater 24 (2014) 2421–2440.
[7] L.-w. Shan, L.-q. He, J. Suriyaprakash, L.-x. Yang, Photoelectrochemical (PEC) water splitting of BiOI {001} nanosheets synthesized by a simple chemical transformation, J. Alloys Compd. 665 (2016) 158–164.
[8] S. Yoon, J.-H. Lim, B. Yoo, Electrochemical synthesis of cuprous oxide on highly conducting metal micro-pillar arrays for water splitting, J. Alloys Compd. 677 (2016) 66–71.
[9] Z. Bai, Y. Zhang, A $Cu_2O/Cu_2S$-ZnO/CdS tandem photoelectrochemical cell for self-driven solar water splitting, J. Alloys Compd. 698 (2017) 133–140.
[10] W. Zhang, B. Wang, C. Hao, Y. Liang, H. Shi, L. Ao, W. Wang, Au/$Cu_2O$ Schottky contact heterostructures with enhanced photocatalytic activity in dye decomposition and photoelectrochemical water splitting under visible light irradiation, J. Alloys Compd. 684 (2016) 445–452.
[11] S. Mohite, V. Ganbavle, K. Rajpure, Solar photoelectrocatalytic activities of rhodamine-B using sprayed $WO_3$ photoelectrode, J. Alloys Compd. 655 (2016) 106–113.
[12] W. Sun, D. Wang, Z.U. Rahman, N. Wei, S. Chen, 3D hierarchical $WO_3$ grown on $TiO_2$ nanotube arrays and their photoelectrochemical performance for water splitting, J. Alloys Compd. 695 (2017) 2154–2159.
[13] M. Sun, Y. Fang, Y. Kong, X. Yuan, J. Shi, A. Umar, Direct in situ synthesis of $Fe_2O_3$-codoped N-doped $TiO_2$ nanoparticles with enhanced photocatalytic and photo-electrochemical properties, J. Alloys Compd. 705 (2017) 89–97.
[14] C. Yu, S. Dong, J. Zhao, X. Han, J. Wang, J. Sun, Preparation and characterization of sphere-shaped $BiVO_4$/reduced graphene oxide photocatalyst for an augmented natural sunlight photocatalytic activity, J. Alloys Compd. 677 (2016) 219–227.
[15] I. Khan, S. Ali, M. Mansha, A. Qurashi, Sonochemical assisted hydrothermal synthesis of pseudo-flower shaped Bismuth vanadate ($BiVO_4$) and their solar-driven water splitting application, Ultrason. Sonochem. 36 (2017) 386–392.
[16] X. Lin, D. Xu, J. Zheng, M. Song, G. Che, Y. Wang, Y. Yang, C. Liu, L. Zhao, L. Chang, Graphitic carbon nitride quantum dots loaded on leaf-like $InVO_4$/$BiVO_4$ nanoheterostructures with enhanced visible-light photocatalytic activity, J. Alloys Compd. 688 (2016) 891–898.
[17] A.Y. Malkhasian, Synthesis and characterization of Pt/$AgVO_3$ nanowires for degradation of atrazine using visible light irradiation, J. Alloys Compd. 649 (2015) 394–399.
[18] P. Wang, H. Tang, Y. Ao, C. Wang, J. Hou, J. Qian, Y. Li, In-situ growth of $Ag_3VO_4$ nanoparticles onto BiOCl nanosheet to form a heterojunction photocatalyst with enhanced performance under visible light irradiation, J. Alloys Compd. 688 (2016) 1–7.
[19] L. Zhou, Q. Yan, A. Shinde, D. Guevarra, P.F. Newhouse, N. Becerra-Stasiewicz, S.M. Chatman, J.A. Haber, J.B. Neaton, J.M. Gregoire, High throughput discovery of solar fuels photoanodes in the CuO-$V_2O_5$ system, Adv. Energy Mater 5 (2015) 1500968.
[20] Q. Yan, G. Li, P.F. Newhouse, J. Yu, K.A. Persson, J.M. Gregoire, J.B. Neaton, $Mn_2V_2O_7$: An earth abundant light absorber for solar water splitting, Adv. Energy Mater 5 (2015) 1401840.
[21] J.A. Seabold, N.R. Neale, All first row transition metal oxide photoanode for water splitting based on $Cu_3V_2O_8$, Chem. Mater 27 (2015) 1005–1013.
[22] F. Wang, H. Zhang, L. Liu, B. Shin, F. Shan, Synthesis, surface properties and optical characteristics of $CuV_2O_6$ nanofibers, J. Alloys Compd. 672 (2016) 229–237.
[23] A. Jezierski, J. Kaczkowski, Electronic structure and thermodynamic properties of $Cu_3V_2O_8$ compound, Phase Trans. 88 (2015) 970–978.
[24] D. Cardenas-Morcoso, A. Peiro-Franch, I. Herraiz-Cardona, S. Gimenez, Chromium doped copper vanadate photoanodes for water splitting, Catal. Today (2016), http://dx.doi.org/10.1016/j.cattod.2016.1011.1002.
[25] W. Guo, W.D. Chemelewski, O. Mabayoje, P. Xiao, Y. Zhang, C.B. Mullins, Synthesis and characterization of $CuV_2O_6$and $Cu_2V_2O_7$: two photoanode candidates for photoelectrochemical water oxidation, J. Phys. Chem. C 119 (2015) 27220–27227.
[26] T. Kawada, S. Hinokuma, M. Machida, Structure and $SO_3$ decomposition activity of nCuO–$V_2O_5/SiO_2$ (n= 0, 1, 2, 3 and 5) catalysts for solar thermochemical water splitting cycles, Catal. Today 242 (2015) 268–273.
[27] P.P. Sahoo, B. Zoellner, P.A. Maggard, Optical, electronic, and photoelectrochemical properties of the p-type $Cu_{3-x}VO_4$ semiconductor, J. Mater. Chem. A 3 (2015) 4501–4509.
[28] L. Zhou, Q. Yan, J. Yu, R.J. Jones, N. Becerra-Stasiewicz, S.K. Suram, A. Shinde, D. Guevarra, J.B. Neaton, K.A. Persson, Stability and self-passivation of copper vanadate photoanodes under chemical, electrochemical, and photoelectrochemical operation, Phys. Chem. Chem. Phys. 18 (2016) 9349–9352.
[29] S. Zhang, W. An, G. Wu, $Cu_5(VO_4)_2(OH)_4 \cdot H_2O$ nanobelts as anode materials for lithium-ion batteries, Chem. Phys. Lett. 621 (2015) 1–4.
[30] J.-q. Cao, X.-y. Wang, A. Tang, X. Wang, Y. Wang, W. Wu, Sol–gel synthesis and electrochemical properties of $CuV_2O_6$ cathode material, J. Alloys Compd. 479 (2009) 875–878.
[31] M.G. Mali, H. Yoon, M.-w. Kim, M.T. Swihart, S.S. Al-Deyab, S.S. Yoon, Electrosprayed heterojunction $WO_3/BiVO_4$ films with nanotextured pillar structure for enhanced photoelectrochemical water splitting, Appl. Phys. Lett. 106 (2015) 151603.
[32] T. Kawada, T. Tajiri, H. Yamashita, M. Machida, Molten copper hexaoxodivanadate: an efficient catalyst for SO 3 decomposition in solar thermochemical water splitting cycles, Catal. Sci. Technol. 4 (2014) 780–785.
[33] H. Ma, S. Zhang, W. Ji, Z. Tao, J. Chen, α-CuV2O6 nanowires: hydrothermal synthesis and primary lithium battery application, J. Am. Chem. Soc. 130 (2008) 5361–5367.
[34] P.F. Newhouse, D. Boyd, A. Shinde, D. Guevarra, L. Zhou, E. Soedarmadji, G. Li, J. Neaton, J. Gregoire, Solar fuel photoanodes prepared by inkjet printing of copper vanadates, J. Mater. Chem. A 4 (2016) 7483–7494.
[35] R. Saito, Y. Miseki, K. Sayama, Highly efficient photoelectrochemical water splitting using a thin film photoanode of $BiVO_4/SnO_2/WO_3$ multi-composite in a carbonate electrolyte, Chem. Commun. 48 (2012) 3833–3835.
[36] J.C. Hill, K.-S. Choi, Effect of electrolytes on the selectivity and stability of n-type $WO_3$ photoelectrodes for use in solar water oxidation, J. Phys. Chem. C 116 (2012) 7612–7620.
[37] H. Yoon, M.G. Mali, M.-w. Kim, S.S. Al-Deyab, S.S. Yoon, Electrostatic spray deposition of transparent tungsten oxide thin-film photoanodes for solar water splitting, Catal. Today 260 (2016) 89–94.